

Higher-order correlation functions in disordered media: Computational algorithms and application to two-phase heterogeneous materials

Hessam Malmir

Department of Chemical and Environmental Engineering, Yale University, New Haven, Connecticut 06511, USA

Muhammad Sahimi*

Mork Family Department of Chemical Engineering and Materials Science, University of Southern California, Los Angeles, California 90089, USA

Yang Jiao

School for Engineering of Matter, Transport and Energy, Arizona State University, Tempe, Arizona 85287, USA



(Received 31 July 2018; revised manuscript received 3 December 2018; published 28 December 2018)

Macroscopic properties of heterogeneous materials, including thermal and electrical conductivity, elastic moduli, and fluid permeability, depend crucially on their microstructure. Optimal design of such materials with desired properties, as well as characterization of their microstructure, are fundamental problems that have been studied for a long time. Accurate characterization of the microstructure is possible if several n -point correlation functions that describe their statistical properties can be computed. While the limits $n = 1$, corresponding to phase fractions, and $n = 2$, that represents such two-point correlation functions as the radial distribution function, have yielded useful information and insights and have been utilized for reconstruction of models of heterogeneous materials, in many cases higher-order correlation functions are required in order to develop deeper understanding of materials' properties, as well as obtaining accurate estimates for them. We describe an algorithm for computing third-order correlation functions. We test the accuracy of the algorithm for a model of fully penetrable disks, i.e., the so-called cherry-pit model in the limit of the penetrability parameter $\lambda = 0$, for which an exact expression for the three-point probability function $S_3(\mathbf{x}_1, \mathbf{x}_2, \mathbf{x}_3)$ is known. Excellent agreement between the computed results and the theoretical predictions is demonstrated. We then report on the results of extensive computations for several types of heterogeneous materials and the analysis of their three-point correlation functions. They include the probability and cluster functions S_3 and C_3 , as well as the three-point surface and surface-surface-void correlation functions F_{sss} and F_{ssv} , for a variety of two- and three-dimensional disordered materials and media.

DOI: [10.1103/PhysRevE.98.063317](https://doi.org/10.1103/PhysRevE.98.063317)

I. INTRODUCTION

Multiphase heterogeneous materials, both natural and man-made, are ubiquitous [1,2]. They are either composed of several constituents, such as composite solids, or of components in different states, such as polycrystals. Examples include concrete [3], sandstone and other types of porous formations [4,5], block copolymers [6], biological tissues [7], membranes [8–10], and many more. Thus, characterization and modeling of heterogeneous materials and media have been problems of great interest, and have been studied for decades. Advances in instrumentation, development of highly efficient computational algorithms, coupled with the dramatic rise in computational speed and memory, and the application of powerful analytical methods to such problems have all contributed to significant progress in characterization and modeling of heterogeneous materials.

While characterization of microstructure of heterogeneous materials has its own high importance, the link between the

microstructure and macroscopic effective properties of such materials, such as diffusivity, electrical, thermal, and magnetic conductivity, permeability, the reaction rate, elastic moduli, and fracture propagation [11] has also motivated much research in this active area. Development of accurate models of heterogeneous materials based on the information and insights obtained from their microstructure will not only lead to precise estimation and/or computation of their macroscopic properties, but also help designing a new class of materials with desired optimal physical properties [12–15].

Systematic characterization of the microstructure of heterogeneous materials relies on the details of their morphology, including the volume fractions of their constituents, surface areas at the interface between their phases or constituents, and the orientations, shapes, sizes, connectivity, and the spatial distributions of their various components. Due to the complexity and seemingly random microstructure of heterogeneous materials, use of statistical methods for their characterization is not only natural, but also necessary. Thus, many n -point correlation functions have been proposed and developed in order to carry out statistical characterization of disordered materials. Such correlation functions arise naturally when one

*moe@usc.edu

attempts to obtain estimates of the macroscopic properties by averaging over the materials' microstructure. The type and complexity of the correlation functions depend on the particular properties that one wishes to study. In some cases, second-order correlation functions, such as the radial distribution function, yield useful information and help constructing accurate models [15,16]. In other cases, two-point correlation functions do not suffice, and the accuracy of the characterization and that of the models that are constructed based on them must be significantly improved through higher-order correlation functions that provide statistical information on the correlations between three and more reference points in the materials. This is particularly true about the problem of reconstruction [16–45] in which one attempts to construct a model of a heterogeneous material or medium based on limited data that not only honors the data, but also provides accurate predictions for its macroscopic properties.

Theoretically, higher-order correlation functions are defined as the expected value of more than two stochastic variables. Although two-point correlation functions are not difficult to compute and many of them are amenable to direct experimental measurements, the same is not true about higher-order correlations. They are rather difficult to compute, measure, and analyze, but if they are available, they can provide very useful information and estimates for various properties. A good example is approximation of the effective diffusion coefficient D [46], which is a function of a three-point microstructural parameter ζ_2 [1,2] that itself is expressed in terms of integrals over the three-point probability function S_3 and its associated lower-order correlations S_2 and S_1 (see below).

There are some analytical approaches for computing the n -point probability function S_n (see below) in heterogeneous materials. Lu and Torquato [47] introduced a series representation of S_n for a lattice model of disordered media. Baniassadi *et al.* [48] proposed an approximate solution for the n -point correlation functions based on a connection between subsets of the $(n-1)$ -point correlation functions. Generally speaking, however, a computational framework for computing various higher-order ($n > 2$) correlation functions in heterogeneous media is crucial, but also not well developed.

In this paper we describe an algorithm for computing higher-order correlations that may be used for accurate characterization of various two- and three-dimensional (2D and 3D) microstructures, including the three-point probability and cluster functions S_3 and C_3 , respectively, as well as the three-point surface correlations F_{ss} and F_{ssv} . We then use the algorithms to compute the functions for a variety of 2D and 3D materials, including packings of overlapping and nonoverlapping disks, ceramics, and Pb-Sn alloy. In the special case of packings of fully penetrable spheres, we benchmark our simulation algorithm and results against the existing analytical solutions. In addition, all the lower-order correlation functions are also computed for the same materials, and compared with the higher-order ones.

The rest of the paper is organized as follows. In Sec. II the theoretical foundation for the higher-order correlation functions is described. Furthermore, computational algorithms are presented for the calculation of the three-point correlation functions in 2D and 3D heterogeneous materials. The

computed results are then presented and discussed in Sec. III. In Sec. IV the computational efficiency of the algorithms is described. Section V presents a discussion of the significance of the higher-order correlation functions, and in particular their link with the transport properties of heterogeneous media. The paper is summarized in Sec. VI.

II. HIGHER-ORDER CORRELATION FUNCTIONS

The higher-order correlation functions that we study in this paper include the three-point probability and cluster functions, as well as the three-point surface correlation functions. In what follows, we describe the theoretical bases for the correlation functions.

A. n -point correlation functions

The n -point probability function $S_n^{(i)}$ for a phase i of a multiphase material is defined as the probability of finding n reference points at spatial positions $\mathbf{x}_1, \mathbf{x}_2, \dots, \mathbf{x}_n$, all in phase i of a heterogeneous multiphase material. The equation for $S_n^{(i)}$, which is of great importance to microstructural characterization and properties of heterogeneous media, is given by

$$S_n^{(i)}(\mathbf{x}^n) = \left\langle \prod_{j=1}^n \mathcal{I}^{(i)}(\mathbf{x}_j) \right\rangle, \quad (1)$$

where $\mathbf{x}^n \equiv \{\mathbf{x}_1, \mathbf{x}_2, \dots, \mathbf{x}_n\}$, and $\mathcal{I}^{(i)}$ is an indicator function for phase i , defined by

$$\mathcal{I}^{(i)}(\mathbf{x}) = \begin{cases} 1 & \text{if } \mathbf{x} \in \mathcal{V}_i, \\ 0 & \text{otherwise,} \end{cases} \quad (2)$$

in which \mathcal{V}_i is the region of phase i with volume fraction of ϕ_i . The limits $n = 1$ and 2 yield one- and two-point probability functions $S_1^{(i)}(\mathbf{x})$ and $S_2^{(i)}(\mathbf{x}_1, \mathbf{x}_2)$, which have been computed and measured for many materials, while $S_3^{(i)}(\mathbf{x}_1, \mathbf{x}_2, \mathbf{x}_3)$ represents the probability of finding three reference points at $\mathbf{x}_1, \mathbf{x}_2$, and \mathbf{x}_3 in the same phase i . For statistically homogeneous and isotropic materials, i.e., when the correlation functions are independent of the coordinate system of translation and rotation, the three-point correlation functions depend only on the distances between the vertices of the triangle ($r_1 \equiv |\mathbf{x}_1 - \mathbf{x}_2|$, $r_2 \equiv |\mathbf{x}_1 - \mathbf{x}_3|$, and $r_3 \equiv |\mathbf{x}_2 - \mathbf{x}_3|$) and, thus,

$$S_3^{(i)}(\mathbf{x}_1, \mathbf{x}_2, \mathbf{x}_3) = S_3^{(i)}(r_1, r_2, r_3) = S_3^{(i)}(r_1, r_2, \theta), \quad (3)$$

where $\theta = \cos^{-1}[(r_1^2 + r_2^2 - r_3^2)/2r_1r_2]$. $S_3^{(i)}$ satisfies the following limiting properties:

$$S_3^{(i)}(r, 0, \theta) = S_3^{(i)}(r, r, 0) = S_2^{(i)}(r). \quad (4)$$

One also has $\lim_{r \rightarrow 0} S_2^{(i)}(r) = S_1^{(i)} = \phi_i$ and $\lim_{r \rightarrow \infty} S_2^{(i)}(r) = \phi_i^2$, with ϕ_i being the volume fraction of phase i . Hence, $\lim_{r_1, r_2 \rightarrow 0} S_3^{(i)}(r_1, r_2, \theta) = \phi_i$ and $\lim_{r_1, r_2 \rightarrow \infty, \theta \neq 0} S_3^{(i)}(r_1, r_2, \theta) = \phi_i^3$ are the additional limits for the three-point probability function.

The following relation holds for the n -point probability function of phase 2 of a two-phase material:

$$S_n^{(2)}(\mathbf{x}^n) = \left\langle \prod_{j=1}^n [1 - \mathcal{I}^{(1)}(\mathbf{x}_j)] \right\rangle, \quad (5)$$

where for a porous medium, for example, superscripts 1 and 2 refer to the pore and solid phases, respectively. Therefore, the three-point probability function in phase 2 (the solid matrix of a porous medium, for example) is obtained from the corresponding function in phase 1 (the pores of the porous medium, for example) via the following equation:

$$S_3^{(2)}(r_1, r_2, r_3) = 1 - 3\phi_1 + S_2^{(1)}(r_1) + S_2^{(1)}(r_2) + S_2^{(1)}(r_3) - S_3^{(1)}(r_1, r_2, r_3). \quad (6)$$

The n -point cluster function $C_n^{(i)}$ is the connectedness analog of the n -point probability function $S_n^{(i)}$. In other words, $C_n^{(i)}(\mathbf{x}_1, \mathbf{x}_2, \dots, \mathbf{x}_n)$ is the probability of finding n reference points at spatial locations $\mathbf{x}_1, \mathbf{x}_2, \dots, \mathbf{x}_n$, all in the same cluster of phase i of a heterogeneous material. For statistically homogeneous and isotropic media, $C_3^{(i)}(r_1, r_2, r_3)$ is the probability of finding three reference points separated by the distances r_1, r_2 , and r_3 in the same cluster of phase i . In fact, C_3 represents a part of S_3 that quantifies the connectedness of phase i of a material and, thus, is a very important microstructural descriptor for the characterization of heterogeneous materials. Similar to $S_3^{(i)}$, $C_3^{(i)}$ is also related to the corresponding two-point connectedness cluster function C_2 :

$$C_3^{(i)}(r, 0, \theta) = C_3^{(i)}(r, r, 0) = C_2^{(i)}(r), \quad (7)$$

with the conditions that $C_2^{(i)}(r) \rightarrow \phi_i$ as $r \rightarrow 0$. $C_2^{(i)}(r) \rightarrow 0$ if $r \rightarrow \infty$ and phase i is not sample spanning. More generally, the cluster functions are not necessarily decreasing functions of positions for percolating phases, especially if the percolating phase is fully connected. Instead, they will plateau to a constant value at sufficiently large distances.

The surface correlation functions contain important interfacial information that determines some of the crucial transport properties of disordered media, including the mean survival time of a diffusant moving among traps distributed in such media, and the fluid permeability [1,2]. Moreover, the surface correlation functions may be used in the reconstruction of heterogeneous media. By far, the only lower-order surface correlation functions that have been computed are F_{ss} and F_{sv} [1,49], but there exists critical need for developing efficient algorithms for computing higher-order surface correlation functions of complex multiphase materials. The general form of the n -point surface correlation functions is expressed by

$$F_{ss\dots svv\dots v}(\mathbf{x}^m; \mathbf{x}^{n-m}) = \left\langle \left[\prod_{i=1}^m \mathcal{M}(\mathbf{x}_i) \right] \left[\prod_{j=m+1}^n \mathcal{I}^{(1)}(\mathbf{x}_j) \right] \right\rangle, \quad (8)$$

with $\mathbf{x}^{n-m} \equiv \mathbf{x}_{m+1}, \mathbf{x}_{m+2}, \dots, \mathbf{x}_n$, and $\mathcal{M}(\mathbf{x}) = |\nabla \mathcal{I}^{(1)}(\mathbf{x})| = |\nabla \mathcal{I}^{(2)}(\mathbf{x})|$ refers to the two-phase interface indicator function. The three-point surface correlation functions F_{sss} and F_{ssv} are then defined by

$$F_{sss}(r_1, r_2, \theta) = \langle \mathcal{M}(\mathbf{x}_1) \mathcal{M}(\mathbf{x}_2) \mathcal{M}(\mathbf{x}_3) \rangle \quad (9)$$

and

$$F_{ssv}(r_1, r_2, \theta) = \langle \mathcal{M}(\mathbf{x}_1) \mathcal{M}(\mathbf{x}_2) \mathcal{I}^{(1)}(\mathbf{x}_3) \rangle \quad (10)$$

with the following limiting behavior:

$$\begin{cases} \lim_{r_2 \rightarrow 0} F_{sss}(r_1, r_2, \theta) = F_{ss}(r_1), \\ \lim_{\substack{r_2 \rightarrow r_1 \\ \theta \rightarrow 0}} F_{sss}(r_1, r_2, \theta) = F_{ss}(r_1). \end{cases} \quad (11)$$

The specific surface s , defined as the interfacial area per unit volume, of a two-phase (or porous) material is given by $s = \langle \mathcal{M}(\mathbf{x}) \rangle$, with $\lim_{r \rightarrow \infty} F_{ss}(r) = s^2$. As $r_1, r_2 \rightarrow \infty$, when $\theta \neq 0$, $F_{sss}(r_1, r_2, \theta) \rightarrow s^3$. In addition, based on the definition of F_{ssv} , one has the following relations for the surface-surface-void correlation function:

$$F_{ssv}(r_1, r_2, \theta) = \begin{cases} F_{sv}(r_1), & r_2 \rightarrow 0 \\ 0, & r_1 \rightarrow 0 \\ 0, & r_2 \rightarrow r_1, \theta \rightarrow 0. \end{cases} \quad (12)$$

Hence, $\lim_{r_1 \rightarrow \infty, r_2 \rightarrow 0} F_{ssv}(r_1, r_2, \theta) = s\phi_1$ and $\lim_{r_1, r_2 \rightarrow \infty, \theta \neq 0} F_{ssv}(r_1, r_2, \theta) = s^2\phi_1$ are the other limiting properties of the surface-surface-void correlation function. For a porous medium, the volume fraction ϕ_1 is usually its porosity ϕ , which means that if either s or $\phi_1 = \phi$ is known, then from the limiting values of $F_{sv}(r)$ as $r \rightarrow \infty$, the other one can be determined.

Most of the aforementioned correlation functions are expressed in terms of a canonical function H_n , defined based on the space and surface available to a test particle inserted in the material [1,2]. For example, adding p test particles of radius b_i to a system of N identical spherical inclusions of radius R with the condition that $p \ll N$, the available space \mathcal{D}_i to the i th test particle would be the space outside N spheres of radius $a_i = b_i + R$ centered at \mathbf{r}^N . Moreover, the available surface \mathcal{S}_i would be the surface between the available space \mathcal{D}_i and its complementary unavailable space \mathcal{D}_i^* , with $\mathcal{V} = \mathbf{D}_i \cup \mathcal{D}_i^*$ being the space in Re^d occupied by a d -dimensional heterogeneous medium. If m of the p test particles are placed on the available surfaces $\mathcal{S}_1, \mathcal{S}_2, \dots, \mathcal{S}_m$, and the rest of the particles lie inside the available spaces $\mathcal{D}_{m+1}, \mathcal{D}_{m+2}, \dots, \mathcal{D}_p$, then, for any q inclusions one defines the canonical function $H_n(\mathbf{x}^m; \mathbf{x}^{p-m}; \mathbf{r}^q)$, in which $\mathbf{x}^m = \{\mathbf{x}_1, \mathbf{x}_2, \dots, \mathbf{x}_m\}$ refers to the centers of the test particles on the available surfaces, $\mathbf{x}^{p-m} = \{\mathbf{x}_{m+1}, \mathbf{x}_{m+2}, \dots, \mathbf{x}_p\}$ denotes the test particles' centers in the available spaces, and $n = p + q$. As a result, the n -point probability function S_n is expressed in terms of the canonical function H_n , when all the reference points, i.e., all the test particles with radii $b_i \rightarrow 0$, lie inside the available space of the medium:

$$S_n(\mathbf{x}^n) = \lim_{a_i \rightarrow R, \forall i} H_n(\emptyset; \mathbf{x}^n; \emptyset). \quad (13)$$

Furthermore, the general form of the surface correlation functions is expressed by

$$F_{ss\dots svv\dots v}(\mathbf{x}^m; \mathbf{x}^{p-m}) = \lim_{a_i \rightarrow R, \forall i} H_n(\mathbf{x}^m; \mathbf{x}^{p-m}; \emptyset), \quad (14)$$

where m and $p - m$ refer, respectively, to the number of the reference points on the surface and in the void region. The

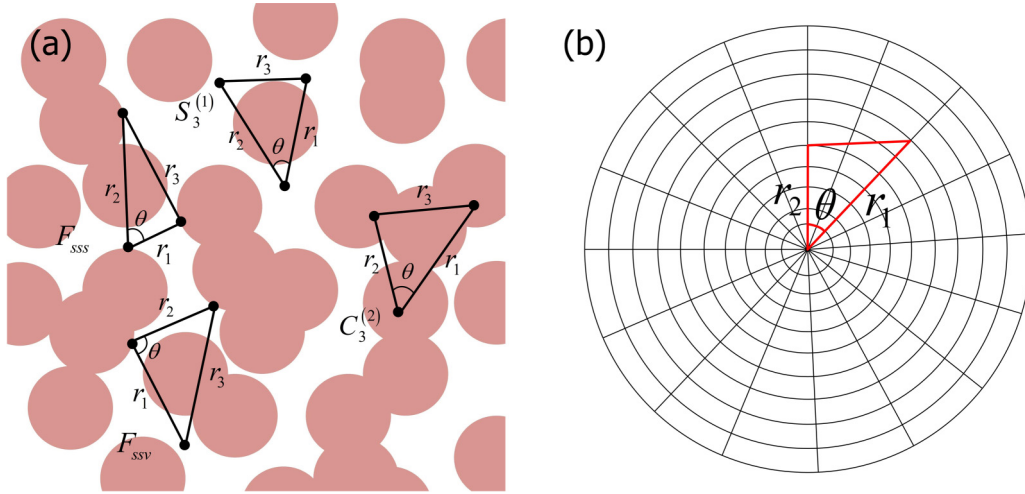


FIG. 1. (a) Schematic representation of the three-point correlation functions. For statistically homogeneous and isotropic media, the functions depend only on the relative distances between the vertices of the triangle r_1 , r_2 , and r_3 . (b) Sampling template for the three-point correlation functions in 2D statistically homogeneous and isotropic media [50].

three-point probability function and surface correlation functions are then expressed in terms of the three-point canonical function H_3 in the limit $a_j \rightarrow R$ ($j = 1, 2$, and 3):

$$S_3(\mathbf{x}_1, \mathbf{x}_2, \mathbf{x}_3) = H_3(\emptyset; \{\mathbf{x}_1, \mathbf{x}_2, \mathbf{x}_3\}; \emptyset), \quad (15)$$

$$F_{ssv}(\mathbf{x}_1, \mathbf{x}_2, \mathbf{x}_3) = H_3(\{\mathbf{x}_1, \mathbf{x}_2, \mathbf{x}_3\}; \emptyset; \emptyset), \quad (16)$$

$$F_{ssv}(\mathbf{x}_1, \mathbf{x}_2, \mathbf{x}_3) = H_3(\{\mathbf{x}_1, \mathbf{x}_2\}; \{\mathbf{x}_3\}; \emptyset). \quad (17)$$

Thus, calculation of the three-point correlation functions will immediately lead to information on the three-point canonical function H_3 , and vice versa.

B. Computational algorithms

The computation of the three-point correlation functions is based on constructing random triangles with vertices at \mathbf{x}_1 , \mathbf{x}_2 , and \mathbf{x}_3 , or with the two sides of lengths r_1 and r_2 along with the angle θ between them; see Fig. 1. We describe two algorithms for computing the three-point correlation functions. One is proposed here, while the second one was developed by Smith and Torquato [50]. In the first approach, one generates a triangle with the side lengths of r_1 and r_2 meeting at vertex \mathbf{x}_1 in the medium, and the angle θ between them. Since for statistically homogeneous and isotropic media the three-point

correlation functions depend only on the relative distances r_1 , r_2 , and r_3 between the triangles' vertices, the position of \mathbf{x}_1 is selected randomly.

In general, for 3D materials, (i) we generate at random the three coordinates $x_1 \in [0, x_{\max}]$, $y_1 \in [0, y_{\max}]$, and $z_1 \in [0, z_{\max}]$ of the main vertex of the triangle at \mathbf{x}_1 . (ii) The other two vertices of the triangle are placed at $\mathbf{x}_2 = (x_1 + r_1, y_1, z_1)$ and $\mathbf{x}_3 = (x_1 + r_2 \cos \theta, y_1 + r_2 \sin \theta, z_1)$. (iii) The triangle is rotated using a quaternion \mathbf{q} , generated by the randomly selected rotating angle $\alpha \in [0, 2\pi)$ around a random unit vector $\mathbf{u} = (u_x, u_y, u_z)$, where $(u_x, u_y, u_z) \in [0, 1]$. Quaternions [51] represent a convenient mathematical notation for representing orientations and rotations of 3D objects. They are simpler to compose than the Euler angles that are used to describe the orientation of a rigid body; avoid losing one degree of freedom (the so-called gimbal lock problem [52]); are more compact than the rotation matrices and more stable numerically, and their use is more efficient. The quaternion for the present problem is given by

$$\mathbf{q} = \cos(\alpha/2) + (u_x \mathbf{i} + u_y \mathbf{j} + u_z \mathbf{k}) \sin(\alpha/2), \quad (18)$$

with \mathbf{i} , \mathbf{j} , and \mathbf{k} being the unit vectors along the Cartesian coordinates. The quaternion-derived rotation matrix \mathbf{R} is then used to rotate the random triangles in 3D space, with \mathbf{R} given by

$$\mathbf{R} = \begin{bmatrix} a^2 + b^2 - c^2 - d^2 & 2(bc - ad) & 2(bd + ac) \\ 2(bc + ad) & a^2 - b^2 + c^2 - d^2 & 2(cd - ab) \\ 2(bd - ac) & 2(cd + ab) & a^2 - b^2 - c^2 + d^2 \end{bmatrix}, \quad (19)$$

where $a = \cos(\alpha/2)$, $b = u_x \sin(\alpha/2)$, $c = u_y \sin(\alpha/2)$, and $d = u_z \sin(\alpha/2)$. Note that the unit vector \mathbf{u} passes through the main vertex of the triangle at \mathbf{x}_1 , and that the initial randomly selected position for \mathbf{x}_1 remains unchanged. (iv) The rotated triangle will be accepted if its other two vertices are also in the medium. Otherwise, we return to step (i) to generate another

triangle to rotate, until all of its vertices are in the medium. (v) We continue all the previous steps for N different sample triangles. The algorithm for 2D media is a specific case for the method that we described in which all the steps are the same, except that in steps (i) and (ii) $z_1 = 0$, and in step (iii) the unit vector \mathbf{u} is equal to $\mathbf{k} = (0, 0, 1)$.

In the second approach [50], a sampling template consisting of many points, similar to a spider web shown in Fig. 1(b), is randomly tossed throughout the medium. This allows one to have many line segments of variable lengths with one end at the template origin \mathbf{x}_1 . In addition, the orientation is also included in the template. Thus, random selection of a triangle with side lengths of r_1 and r_2 and the angle θ can be done on regular grids in 2D polar or 3D spherical coordinates. Figure 1(b) illustrates a 2D template. Sampling templates at N random locations in the medium leads to N different triangles. Similar to the first approach, there needs to be a test of whether the second and third vertices lie in the medium in order to accept the triangles.

In both approaches $N \gg 1$ of the triangles must be generated and tested whether (i) their vertices are in phase i of the medium, in order to compute the probability function $S_3^{(i)}$; (ii) the vertices are all at the interface between the different phases of the medium in the case of calculation of the three-point surface correlation function F_{sss} ; and (iii) if two vertices are at the interface between two different phases, while the third vertex is in the void region (pore space) to compute the surface-surface-void correlation function F_{ssv} . The percentage of the triangles that satisfy the constraints represents the three-point functions.

The cluster function $C_3^{(i)}$ is the connectedness analog of the probability function $S_3^{(i)}$ and its computation follows the procedure for $S_3^{(i)}$, except that only those triangles whose vertices are all in the same *cluster* of phase i are counted. Thus, one needs to use a cluster-identification algorithm, for which we used the method by Sevick *et al.* [53]. Since all the correlation functions are statistical measures, they must be averaged over M independent calculations for the same configuration (image) or over M different realizations. To compute the results described in the next sections, we used $N = 5000$ sample triangles and averaged over $M = 40$ different calculations.

III. RESULTS

We carried out extensive simulations to compute the three-point correlation functions for several 2D and 3D examples of heterogeneous media, all of which represent two-phase materials that are statistically homogeneous and isotropic. In what follows, we present and discuss the results.

A. Packing of overlapping disks

The first example that we examine is a packing of overlapping spheres, a realization of the well-known cherry-pit model [54] in which each d -dimensional sphere of diameter $D = 2R$ is composed of a hard impenetrable core of diameter $2\lambda R$, encompassed by a perfectly penetrable shell of thickness $(1 - \lambda)R$. The reason we calculated the three-point correlation functions for this model of disordered materials is that we can benchmark our numerical results for S_3 and the surface correlation functions, obtained via the computational algorithms described in the previous section, against analytical expressions for a fully penetrable spheres model that represents the limit $\lambda = 0$. The three-point probability

function S_3 for this case is given by

$$S_3^{(1)}(r_1, r_2, \theta) = \exp \left[-\eta \frac{v_3(r_1, r_2, \theta; R)}{v_1(R)} \right], \quad (20)$$

where $v_1(R)$ is the volume of a d -dimensional sphere (πr^2 and $4/3\pi r^3$ in 2D and 3D, respectively), and $\eta = \rho v_1(R)$ denotes the dimensionless and reduced density, with ρ being the number density of the particles. Here, $v_3(r_1, r_2, \theta; R)$ is referred to as the union volume of three identical d -dimensional spheres of radius R with their centers at the vertices of a triangle with the side lengths of r_1 , r_2 and the angle θ between them. Furthermore, the two-point surface correlation function F_{ss} for fully penetrable spheres is given by

$$F_{ss}(r) = \left\{ \frac{9\eta^2}{R^2} \left[1 - \left(\frac{1}{2} - \frac{r}{4R} \right) \Theta(2R - r) \right]^2 + \frac{3\eta}{2rR} \Theta(2R - r) \right\} S_2^{(1)}(r), \quad (21)$$

where $\Theta(x)$ is the Heaviside step function, and $S_2^{(1)}(r)$ is given by

$$S_2^{(1)}(r) = \exp \left[-\eta \frac{v_2(r; R)}{v_1(R)} \right], \quad (22)$$

in which $v_2(r; R)$ is the union volume of two spheres of radius R at a center-to-center distance r .

We benchmarked the simulation results against Eqs. (20) and (21) for packings of fully penetrable disks, the limit $\lambda = 0$. Figure 2(a) shows the three-point probability function S_3 versus the angle θ for phase 1 (void region) of a packing of fully penetrable disks with the packing fractions of $\phi_2 = 0.5$ and 0.2 (porosities, $\phi_1 = 0.5$ and 0.8 , respectively). In this example, the side lengths r_1 and r_2 were set to be 1 pixel. As illustrated, the simulation results for the two packing fractions are in excellent agreement with the analytical expression. In addition, Fig. 2(b) shows the comparison between our simulation results for the three-point surface correlation function $F_{sss}(r_1, r_1, 0)$, which is equal to $F_{ss}(r_1)$, against the analytical solution for the two-point surface correlation function F_{ss} [Eq. (21)]. Two void fractions, $\phi_1 = 0.5$ and 0.8 , were considered, as for S_3 in Fig. 2(a). As shown, the simulation results for both cases are in excellent agreement with the theoretical expression. As before, at $r_1 = D = 14$ pixels there is a kink in the analytical solution for $F_{ss}(r_1)$ [Eq. (21)], which is completely reproduced by the simulations.

Figure 3(a) presents a 2D 150²-pixel realization of a packing of overlapping disks, the cherry-pit model, with $\lambda = 0.5$, which is a model porous medium with porosity $\phi = \phi_1 \approx 0.52$, or a packing fraction ϕ_2 of 0.48. The diameter D of the disks is equivalent to 14 pixels. Hence, the pixel sizes are as small as $\frac{1}{14}$ of the diameter of one disk.

The computed probability function S_3 for phase 1, the pore phase, is presented in Figs. 3(b), 3(c), and 3(d), with Fig. 3(b) showing the top view of the surface plot of the function for $\theta = 0$. As Eq. (4) indicates, on the axis $r_2 = 0$, as well as on the principal diagonal of the square matrix of Fig. 3(b), $S_3^{(1)}(r_1, r_2, 0) = S_2^{(1)}$. Furthermore, the lowest value of the color map of $S_3^{(1)}(r_1, r_2, 0)$ in Fig. 3(b) refers to $\phi_1^3 \approx 0.14$, satisfying the theoretical expectations.

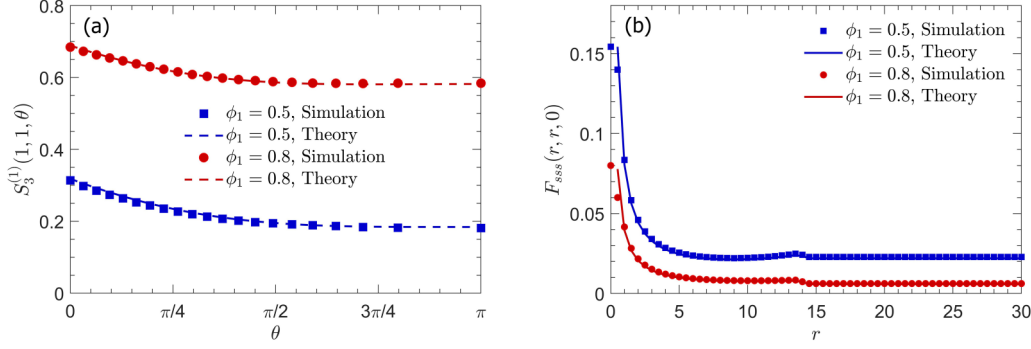


FIG. 2. (a) The probability function $S_3^{(1)}$ for $r_1 = r_2 = 1$, computed by the proposed algorithm, and its comparison with the analytical expression for packings of fully penetrable disks with void fraction of ϕ_1 (packing fraction of $\phi_2 = 1 - \phi_1$). The error bars represent 10 standard deviations. (b) The surface correlation function $F_{sss}(r, r, 0) = F_{ss}(r)$ (for $r_1 = r_2 = r$), computed by the algorithm, and its comparison with the analytical solutions for F_{ss} [Eq. (21)] for packings of fully penetrable disks with void fraction ϕ_1 . At $r = D = 14$ pixels there is a kink in the exact analytical expression for $F_{ss}(r)$, which is accurately reproduced by the simulations.

Figures 3(c) and 3(d) indicate that there is no evidence for oscillatory behavior of the correlation function, hence manifesting some sort of disorder in the packing. The minimum value of the curves occurs at $r_1 = D$, where D is the diameter of the disks, equivalent to 14 pixels in this example. In Fig. 3(c) we present $S_3^{(1)}(r_1, r_2, \pi/2)$ for several values of r_2 , while Fig. 3(d) presents the angle dependence of $S_3^{(1)}(r_1, r_2, \theta)$ with $r_2 = r_1$, i.e., on the principal diagonal of $S_3^{(1)}$. As Eq. (4) indicates, $S_3^{(1)}(r_1, 0, \pi/2) = S_3^{(1)}(r_1, r_1, 0) = S_2^{(1)}(r_1) \equiv S_2^{(1)}(r)$. The computed values for $\lim_{r \rightarrow 0} S_2^{(1)}(r) = \phi_1 \approx 0.52$ and for $\lim_{r \rightarrow \infty} S_2^{(1)}(r) = \phi_1^2 \approx 0.27$ also satisfy the theoretical expectations and, thus, indicate the accuracy of the computations.

Figure 3(e) presents the cluster function $C_3^{(2)}$ for the solid phase in the limit $\theta = \pi/2$, including the limit $r_2 = 0$ in which $C_3^{(2)}(r_1, 0, \pi/2) = C_2^{(2)}$, while $C_3^{(2)}(r_1, r_2, \theta)$ has the same limiting behavior when $r_1 = r_2$ and $\theta = 0$; see Fig. 3(f). As expected, with increasing r_2 or decreasing θ , $C_3^{(2)}$ decreases. However, the dependence of the cluster function $C_3^{(2)}$ on the distance or angle θ provides no clue to the type of the disorder that the packing contains. The computed values $\lim_{r \rightarrow 0} C_2^{(2)}(r) = \phi_2 \approx 0.52$ and $\lim_{r \rightarrow \infty} C_2^{(2)}(r) = 0$ also satisfy the analytical predictions for the two-point cluster function, and also acting as a check of the accuracy of the computations.

The calculated surface correlation function $F_{sss}(r)$ and surface-surface-void correlation function $F_{ssv}(r)$ are plotted in Figs. 3(g) and 3(h), respectively. The former produces correctly the two-point surface correlation function $F_{ss}(r)$ in the limits $r_1 = r_2$ and $\theta = 0$, which is equivalent to the specific surface s at $r_1 = 0$ and s^2 as $r_1 \rightarrow \infty$, while the latter yields $F_{sv}(r)$ in the limits $r_2 = 0$ and $\theta = \pi/2$. For $\theta > 0$, the surface-surface-surface correlation function quickly vanishes with the distance because it is very difficult to find three points at the interface between the two phases to form a triangle, whereas in the limit $\theta = 0$, i.e., when the three points are all on a straight line, F_{sss} quickly approaches its nonzero asymptotic value. On the other hand, it is always possible to find such three points with one being in the void region, which explains why $F_{ssv}(r_1, r_2, \theta)$ quickly approaches its nonzero

asymptotic values, as Fig. 3(h) indicates. Furthermore, the limits $\lim_{r \rightarrow \infty} F_{ss}(r) = s^2$ in Fig. 3(g) and $\lim_{r \rightarrow \infty} F_{sv}(r) = s\phi_1$ in Fig. 3(h) yield consistently an estimate for the specific surface $s \approx 0.08$. We point out again that there exists a kink at $r_1 = D = 14$ for F_{sss} in Fig. 3(g), which is also expected analytically. Note also that the points at the interface between the two phases in the digitized image are the pixels (voxels in 3D) on the boundary between them.

B. Packing of impenetrable disks

The second 2D example whose three-point correlation functions were computed is a 150^2 -pixel realization of a packing of nonoverlapping disks, shown in Fig. 4(a). The packing was generated by the random sequential-adsorption algorithm with periodic boundary conditions, and represents a porous medium with porosity $\phi = \phi_1 \approx 0.48$, or a packing fraction of $\phi_2 \approx 0.52$. Similar to the previous example of the overlapping disks, the pixel sizes are as small as $\frac{1}{14}$ of the diameter of one disk. Figures 4(b), 4(c), and 4(d) present the computed probability function $S_3^{(1)}$ in various limits, with Fig. 4(b) showing the top view of the surface plot of the probability function for $\theta = 0$. Similar to the previous example, on the axis $r_2 = 0$, or on the principal diagonal of the square matrix $S_3^{(1)}(r_1, r_2, 0) = S_2^{(1)}(r)$, which satisfies the conditions in Eq. (4).

The most striking feature of the results for $S_3^{(1)}$, shown in Figs. 4(c) and 4(d), is their oscillatory behavior. A comparison with the corresponding results, in the previous example for the packing of the same disks but with overlapping particles, indicates that such a behavior is due to some degree of order in the material, which the penetrable disks lack. In fact, the oscillating behavior exists for all values of r_2 and θ , and is already indicated by Fig. 4(b), as the distribution of the off-diagonal values of the function is not uniform (in colors). As Eq. (4) indicates, $S_3^{(1)}(r_1, 0, \pi/2) = S_3^{(1)}(r_1, r_1, 0) = S_2^{(1)}(r_1) \equiv S_2^{(1)}(r)$. Once again, the computations yield correctly $\lim_{r \rightarrow 0} S_2^{(1)}(r) = \phi_1 \approx 0.48$ and $\lim_{r \rightarrow \infty} S_2^{(1)}(r) = \phi_1^2 \approx 0.23$, which are theoretically rigorous.

Figures 4(e) and 4(f) present the computed cluster function $C_3^{(2)}$ in various limits. Note that the qualitative trends

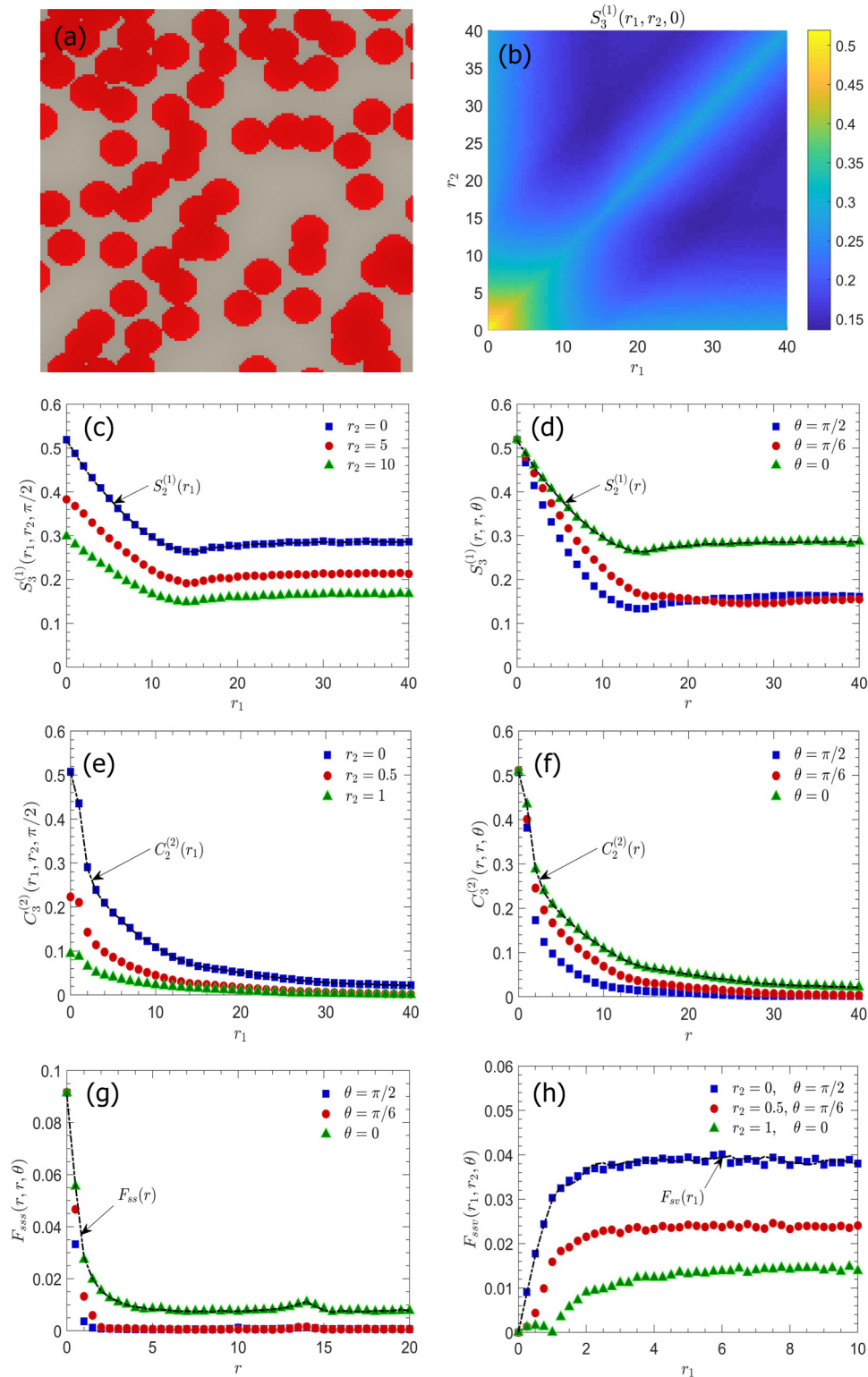


FIG. 3. (a) A (150×150)-pixel realization of a packing of overlapping disks, the 2D cherry-pit model with the penetrability parameter $\lambda = 0.5$ and periodic boundary condition. The pore phase (phase 1) and solid phase (phase 2) are shown by gray and red, respectively. The packing fraction ϕ_2 is ≈ 0.48 . The diameter of the disks D is equivalent to 14 pixels. (b) Top view of the surface plot of the probability function for phase 1 and $\theta = 0$. (c) The probability function $S_3^{(1)}$ versus r_1 for $\theta = \pi/2$. (d) The probability function $S_3^{(1)}$ for $r_2 = r_1 = r$. (e) The cluster function $C_3^{(1)}$ for $\theta = \pi/2$. (f) The cluster function $C_3^{(1)}$ with $r_2 = r_1 = r$. (g) The surface correlation function F_{sss} with $r_2 = r_1 = r$ and various values of θ . (h) The surface-surface-void correlation function F_{ssv} .

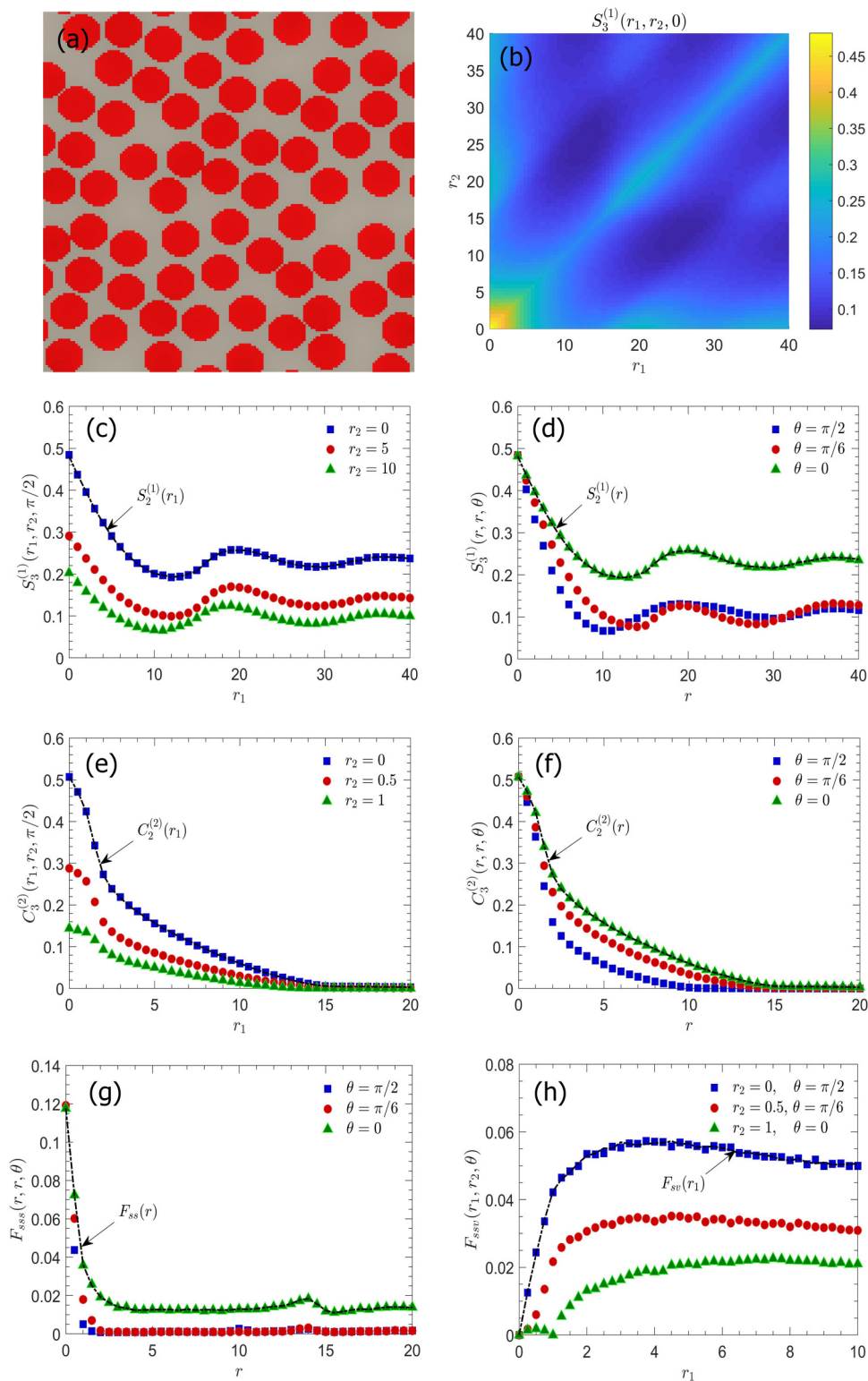


FIG. 4. (a) A (150×150)-pixel realization of a packing of nonoverlapping hard disks with periodic boundary condition. The pore phase (phase 1) and solid phase (phase 2) are shown by gray and red, respectively. The packing fraction ϕ_2 is 0.52. The diameter of the disks D is equivalent to 14 pixels. (b) Top view of the surface plot of the probability function for phase 1 for $\theta = 0$. (c) The probability function $S_3^{(1)}$ versus r_1 with $\theta = \pi/2$, and (d) for $r_2 = r_1 = r$. (e) The cluster function $C_3^{(2)}$ with $\theta = \pi/2$, and (f) for $r_2 = r_1 = r$. (g) The surface correlation function F_{SSS} with $r_2 = r_1 = r$ and various values of θ . (h) The surface-surface-void correlation function F_{SSV} .

and shape of the correlation function C_3 for the packing of overlapping and nonoverlapping disks are completely similar. Thus, although $C_3^{(i)}$ provides insight into the connectivity of the phases of a multiphase material, it does not provide sufficient information about the spatial structure of the phase and the type of disorder or order that a material may contain. As Eqs. (7) indicate, $C_3^{(2)}(r_1, 0, \pi/2) = C_3^{(2)}(r_1, r_1, 0) = C_2^{(2)}(r_1) \equiv C_2^{(2)}(r)$. Moreover, the computed values for $\lim_{r \rightarrow 0} C_2^{(2)}(r) = \phi_2 \approx 0.52$ and $\lim_{r \rightarrow \infty} C_2^{(2)}(r) = 0$ agree with the theoretical expectations.

The calculated surface correlation function $F_{sss}(r)$ and surface-surface-void correlation function $F_{ssv}(r)$ are depicted in Figs. 4(g) and 4(h), with the former showing the principal diagonal of the square matrix $F_{sss}(r_1, r_2, \theta)$ for several values of θ . Similar to the previous example, the theoretical expectations that $F_{sss}(r_1, r_1, 0) = F_{ss}(r_1)$ and $F_{ssv}(r_1, 0, \pi/2) = F_{sv}(r_1)$ are satisfied, and from the two theoretical limits, $\lim_{r \rightarrow \infty} F_{ss}(r) = s^2$ and $\lim_{r \rightarrow \infty} F_{sv}(r) = s\phi_1$, we estimate the specific surface area s to be 0.11. Similar to the previous examples, there exists a kink at $r_1 = D = 14$ for F_{sss} in Fig. 4(g) for overlapping disks, which is expected analytically.

C. Ceramics

As the third 2D example, a 180²-pixel image of a boron-carbide/aluminum (B4C/Al) interpenetrating composite [16], obtained via x-ray microtomography and shown in Fig. 5(a), was considered. It is a two-phase material with the fraction of phase 1 [i.e., the boron-carbide phase represented by gray in Fig. 5(a)] being $\phi_1 = 0.64$. The computed probability function $S_3^{(1)}$ is presented in Figs. 5(b), 5(c), and 5(d). In Fig. 5(b) the top view of the surface plot of the correlation function for $\theta = 0$ is shown. As in the case of previous examples, on the axis $r_2 = 0$, as well as on the principal diagonal of the square matrix, $S_3^{(1)}(r_1, r_2, 0) = S_2^{(1)}$, which are shown in Figs. 5(c) and 5(d). Furthermore, $S_3^{(1)}(r_1, r_2, 0)$ for other values of r_1 and r_2 is uniformly equal to $\phi_1^3 \approx 0.26$, indicating strong disorder in the medium.

In Fig. 5(c), $S_3^{(1)}(r_1, r_2, \pi/2)$ is plotted for several r_2 . Similar to the previous examples, $S_3^{(1)}(r_1, r_2, \pi/2) = S_2^{(1)}(r_1)$ for $r_2 = 0$. Figure 5(d) presents a comparison between $S_3^{(1)}$ for three values of the angle θ , when $r_2 = r_1$. For $\theta = 0$, which corresponds to the case when the two sides of the triangles are along the same line and in the same direction, $S_3^{(1)}(r_1, r_1, 0) = S_2^{(1)}(r_1)$. In addition, as the angle θ increases, $S_3^{(1)}(r_1, r_1, \theta)$ decreases with the same asymptotic value for all $\theta > 0$, indicating that for $\theta > 0$ there is no longer any difference between the values of the diagonal of $S_3^{(1)}(r_1, r_2, \theta)$ with its surrounding values (ϕ_1^3). Note also that the correct limiting values $\lim_{r \rightarrow 0} S_2^{(1)}(r) = \phi_1 \approx 0.65$ and $\lim_{r \rightarrow \infty} S_2^{(1)}(r) = \phi_1^2 \approx 0.44$ are recovered.

Figure 5(e) shows the cluster function $C_3^{(2)}$ for the right triangles ($\theta = \pi/2$) with sides r_1 and r_2 and several values of r_2 . As one expects from Eqs. (7), for $r_2 = 0$, $C_3^{(2)}(r_1, 0, \pi/2) = C_2^{(2)}(r_1)$. Moreover, as r_2 increases, $C_3^{(2)}$ decreases with a pattern similar to that of $S_3^{(1)}$ in Fig. 5(c). Figure 5(f) presents

the cluster function $C_3^{(2)}(r_1, r_1, \theta)$ versus r_1 for various angles θ . As illustrated, $C_3^{(2)}(r_1, r_1, 0) = C_2^{(2)}(r_1)$. Since the cluster function $C_3^{(i)}$ represents a measure of the connectivity of phase i , it is clear that it should decay with increasing distances, except for fully connected phases. Moreover, the computed functions satisfy the rigorous limits $\lim_{r \rightarrow 0} C_2^{(2)}(r) = \phi_1 \approx 0.36$ and $\lim_{r \rightarrow \infty} C_2^{(2)}(r) \rightarrow 0$. The cluster function $C_2^{(i)}(r)$ has been used in the reconstruction of models of disordered materials and media [17,35], and has been shown to yield accurate models.

The calculated three-point surface correlation function $F_{sss}(r)$ and surface-surface-void correlation function $F_{ssv}(r)$ are depicted, respectively, in Figs. 5(g) and 5(h). The former decays with r_1 , as Fig. 5(g) indicates, which shows the principal diagonal of the square matrix $F_{sss}(r_1, r_2, \theta)$ versus r_1 , which is expected. Note that one has $F_{sss}(r_1, r_1, 0) = F_{ss}(r_1)$, which is what Eqs. (11) predict. In contrast with Fig. 5(g), however, Fig. 5(h) that presents $F_{ssv}(r_1, r_2, \theta)$ indicates that the surface-surface-void correlation function increases with the distance since the likelihood that one of the three points is found in the void, or in the second phase of the material, increases with increasing distance. As Eqs. (12) indicate, one has $F_{ssv}(r_1, 0, \theta) = F_{sv}(r_1)$. Since $\lim_{r \rightarrow \infty} F_{ss}(r) = s^2$ and $\lim_{r \rightarrow \infty} F_{sv}(r) = s\phi_1$, the specific surface s obtained from Figs. 5(g) and 5(h) must be equal. Indeed, they both yield $s \approx 0.12$.

D. Pb-Sn Alloy

The fourth example that we analyze is a 3D two-phase heterogeneous material, a Pb63Sn37 alloy with a Eutectic microstructure [40], whose image is shown in Fig. 6(a). It represents a 128³-voxel image, obtained via x-ray microtomography. The volume fraction of phase 1, represented as achromatic in Fig. 6(a), is 0.65. The computed probability function $S_3^{(1)}(r_1, r_2, \theta)$ is presented in Figs. 6(b), 6(c), and 6(d). Similar to the 2D ceramic, the nearly uniform distribution of the off-diagonal values of $S_3^{(1)}(r_1, r_2, 0)$, which is equal to $\phi_1^3 \approx 0.27$ and shown in Fig. 6(b), indicates the existence of strong disorder in the material. As expected based on Eqs. (4), $S_3^{(1)}(r_1, r_2, \pi/2)$ shown in Fig. 6(c) reduces to $S_2^{(1)}(r)$ for $r_2 = 0$, just as $S_3^{(1)}(r_1, r_1, 0) = S_2^{(1)}$, which is what Fig. 6(d) shows. In addition, as θ increases, $S_3^{(1)}(r_1, r_1, \theta)$ decays rapidly, approaching the same asymptotic value for all $\theta > 0$, which is equal to $\phi_1^3 \approx 0.27$. In addition, the computed limiting values $\lim_{r \rightarrow 0} S_2^{(1)}(r) = \phi_1 \approx 0.65$ and $\lim_{r \rightarrow \infty} S_2^{(1)}(r) = \phi_1^2 \approx 0.42$ are in perfect agreement with the theoretical expectations.

In Fig. 6(e) the cluster function $C_3^{(2)}$ is plotted for the right triangles ($\theta = \pi/2$) versus r_1 for several values of r_2 . As one expects from Eqs. (7), for $r_2 = 0$, $C_3^{(2)}(r_1, r_2, \pi/2) = C_2^{(2)}(r_1)$. Moreover, $C_3^{(2)}$ decays with increasing r_1 and r_2 , with trends similar to the results for $S_3^{(1)}$, but unlike $S_3^{(1)}$ it vanishes as $r_1 \rightarrow \infty$. In addition, Fig. 6(f) presents the cluster function $C_3^{(2)}$ versus r_1 for $r_2 = r_1$ and various angles θ . $C_3^{(2)}(r_1, r_1, \theta)$ is equivalent to $C_2^{(2)}(r)$ for $\theta = 0$. Moreover,

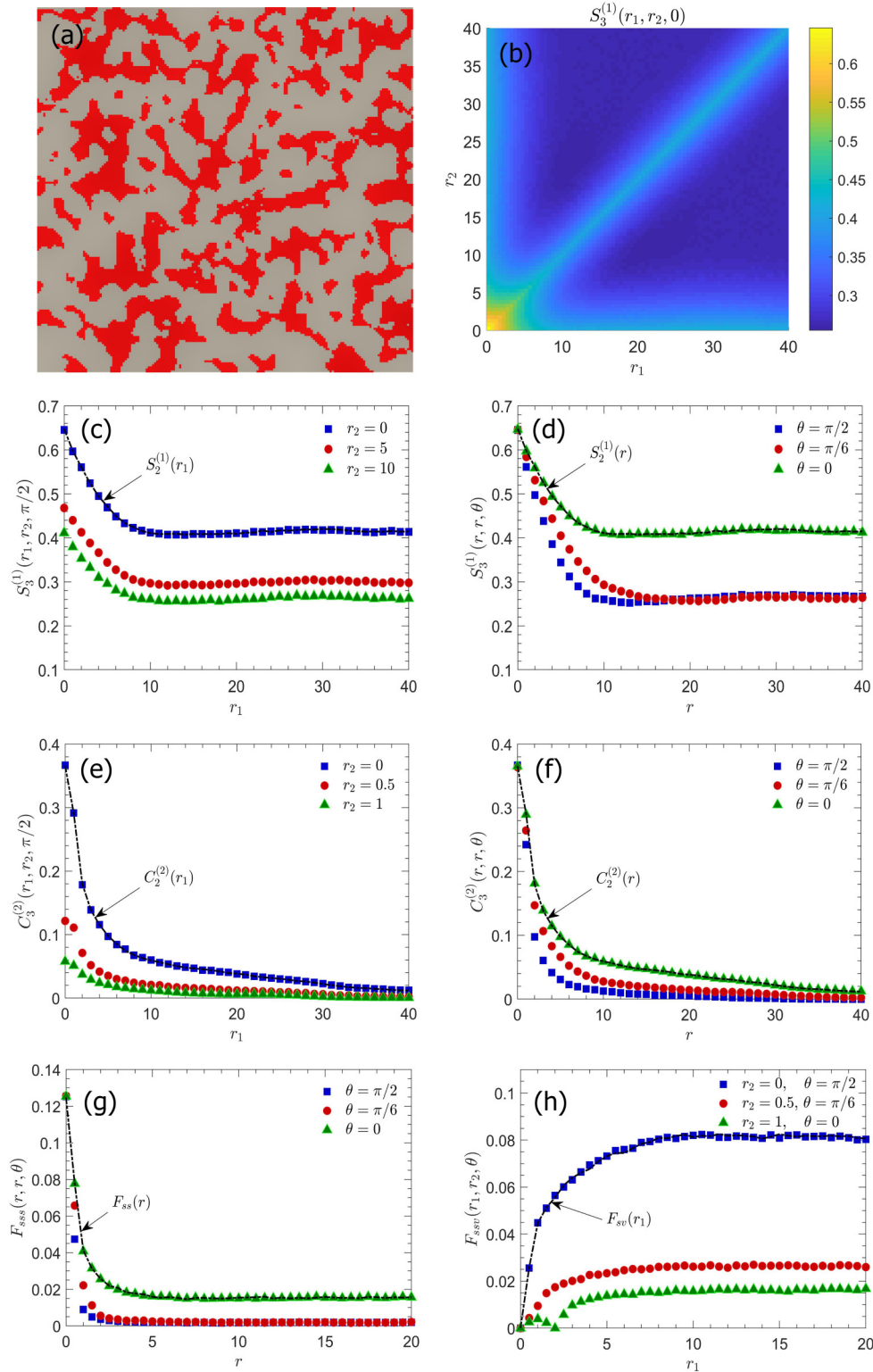


FIG. 5. A (180×180)-pixel image of a ceramic-matrix composite, obtained by x-ray microtomography. The resolution of the system is 1 pixel $\sim 1.5 \mu\text{m}$. Phases 1 (boron-carbide) and 2 (aluminum) are shown by gray and red, respectively. The phase fraction for boron-carbide is $\phi_1 = 0.64$. (b) Top view of the surface plot of the probability function for phase 1 and $\theta = 0$. (c) The probability function $S_3^{(1)}$ versus r_1 for $\theta = \pi/2$. (d) $S_3^{(1)}$ for $r_2 = r_1 = r$. (e) The cluster function $C_3^{(1)}$ with $\theta = \pi/2$, and (f) for $r_2 = r_1 = r$. (g) The surface correlation function F_{ss} for $r_2 = r_1 = r$ and various values of θ . (h) The surface-surface-void correlation function F_{ssv} .

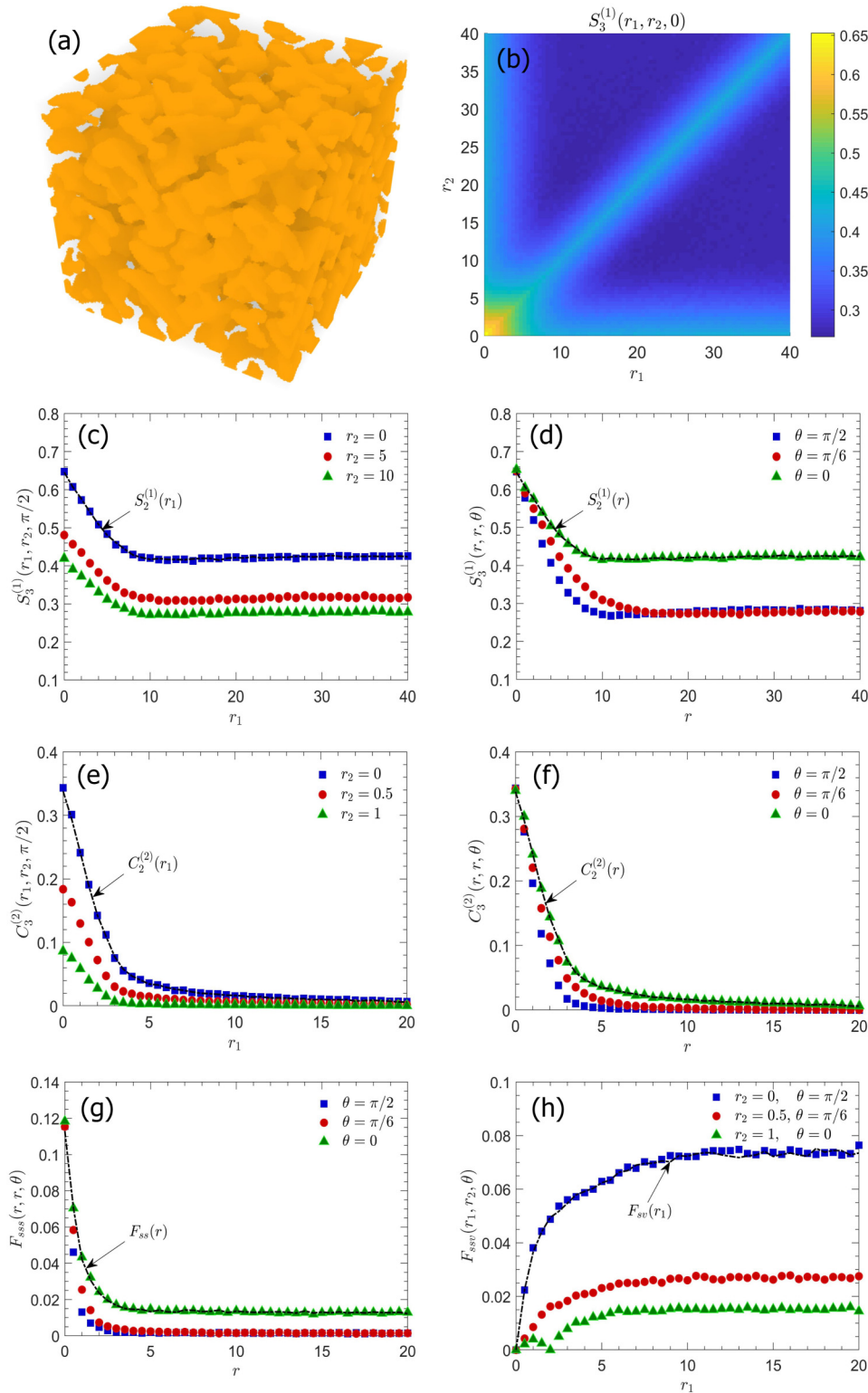


FIG. 6. (a) A $(128 \times 128 \times 128)$ -voxel image of a Pb-Sn alloy. The resolution of the image is 1 pixel $\sim 2.5 \mu\text{m}$. Phase 1 is shown by orange with its volume fraction being $\phi_1 = 0.65$, while phase 2 is achromatic. (b) Top view of the surface plot of the three-point probability function for phase 1 with $\theta = 0$. (c) The probability function $S_3^{(1)}$ versus r_1 for $\theta = \pi/2$, and (d) for $r_2 = r_1 = r$. (e) The cluster function $C_3^{(1)}$ for $\theta = \pi/2$, and for (f) $r_2 = r_1 = r$. (g) The surface correlation function F_{ss} for $r_2 = r_1 = r$ and various values of θ . (h) The surface-surface-void correlation function F_{ssv} .

the computed values do reproduce the theoretical expectations that $\lim_{r \rightarrow 0} C_2^{(2)}(r) = \phi_2 \approx 0.35$ and $C_2^{(2)}(r) \rightarrow 0$ as $r \rightarrow \infty$.

Finally, the computed surface correlation function $F_{ss}(r)$ and surface-surface-void correlation function $F_{ssv}(r)$ are depicted in Figs. 6(g) and 6(h), respectively, with the former reducing to $F_{ss}(r)$ in the limits $r_1 = r_2$ and $\theta = 0$, and the latter to the two-point surface-void correlation function

$F_{sv}(r)$ in the limit $r_2 = 0$ and $\theta = \pi/2$. As in the case of the previous examples, F_{ss} decays rapidly and vanishes for all $\theta > 0$, whereas, for fixed values of r_2 and θ , F_{ssv} increases rapidly with r_1 and approaches a nonzero asymptotic value that depends on r_2 and θ , with $\lim_{r \rightarrow \infty} F_{ss}(r) = s^2$ and $\lim_{r \rightarrow \infty} F_{sv}(r) = s\phi_1$. The two limits together yield an accurate estimate of the specific surface area of the alloy $s \approx 0.11$.

IV. COMPUTATIONAL EFFICIENCY

It is important to discuss and compare the efficiency of the two approaches for computing the three-point correlation functions. For this aim, the CPU times for computing S_3 , F_{sss} , and C_3 for the 180^2 -pixel image of the ceramic as a 2D example and for the 128^3 -voxel image of the Pb-Sn alloy as a 3D example are compared. In both approaches with $N = 5000$ sample triangles and $M = 40$ independent realizations (calculations), the computation of S_3 , F_{sss} , and F_{ssv} on an Intel® Core™ i7-6500U (2.5 GHz) processor took about 1–2 CPU minutes for the 2D example and about 4–5 CPU minutes for the 3D alloy. Computing C_3 is, however, highly dependent on the cluster identification algorithm. If we use the connectivity matrix algorithm, computation of C_3 would take about 2–3 CPU hours for the 2D example and about 7–8 CPU hours for the 3D alloy. Most of the CPU time is, however, devoted to the construction of the connectivity matrix (the cluster-identification part of the computations) and, hence, there is no significant difference between the computation times of C_2 and C_3 in this regard. Consequently, if one uses a more efficient cluster-identification algorithm and hardware with much higher speeds, computing C_3 could take much less time. In that case, C_3 could be incorporated in the reconstruction of models of heterogeneous materials.

V. DISCUSSION

We should first point out that the pixel size of each realization can have measurable effects on the computation of microstructure functions. Thus, the effect of the pixel's size deserves some discussions. We point out that pixelization, i.e., the resolution of the microstructural image, would have significant effect on the correlation functions associated with small values of the distance r , i.e., the small-scale structural features, but that large-scale correlations corresponding to large r should not be very sensitive to the resolution. That our algorithm does capture the kink in the intermediate r values as seen in, for example, Fig. 2(b), supports our claim, but also indicates that the computational algorithm is accurate sensitive to such details.

We also computed the absolute values of the error between the computed correlation function $F_{ss}(r) = F_{sss}(r, r, 0)$ and the predictions of the analytical prediction [Eq. (21)] for each r , for the overlapping disk system with $N = 150$ pixels and diameter $D = 14$ (pixels). Figure 7 presents the plot of the absolute values of the relative error,

$$\text{Relative error} = \left| \frac{\text{computed value} - \text{theoretical prediction}}{\text{theoretical prediction}} \right| \times 100$$

as a function of the distance r . It is clear that the most significant discrepancies between values of the computed function and the theoretical predictions are associated with small values of r , and even at such distances the error is a few percentage. This indicates that even for a very moderate resolution, e.g., 1 pixel $\approx \frac{1}{14}$ particle diameter, the proposed algorithm is sufficiently accurate to capture the true behavior of the correlation functions. Most microstructural images possess very high resolutions. Therefore, we expect the computed

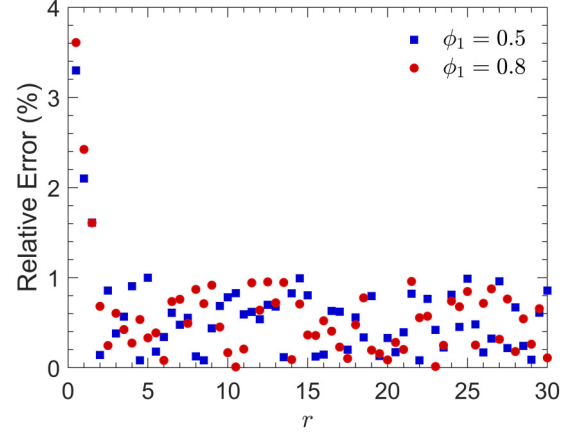


FIG. 7. The absolute values of relative errors in the computed values of the surface correlation function $F_{ss}(r) = F_{sss}(r, r, 0)$ relative to their exact values predicted by Eq. (21).

correlation functions for such images not to be significantly affected by the pixelization.

Having established the accuracy and sensitivity of the proposed algorithm for computing three-point correlation functions, we point out that higher-order probability and correlation functions enable one to characterize more accurately the microstructure of heterogeneous materials, and develop models for them. For example, Tahmasebi and Sahimi [36–39,45] showed that a highly accurate reconstructed model of a heterogeneous material is obtained if one defines a more general cross-correlation function between a region of the model to be reconstructed and the *entire data set* that is available for use in the reconstruction. Higher-order correlation functions may also provide accurate estimates of some of transport properties of disordered materials. Consider, for example, the effective conductivity σ_e and diffusivity D_e of a two-phase disordered material, such as a porous composite solid. Torquato [55] derived an infinite “strong-contrast” series expansion in terms of the contrast between the conductivities or diffusivities of the individual phases. He demonstrated that an approximate but accurate resummation of the series that incorporates up to four-point probability functions involving S_2 , S_3 , and S_4 provide accurate estimates of σ_e and D_e under a variety of conditions. In particular [55],

$$\frac{D_e}{D_1} = \frac{2}{1 - \phi_2} \frac{(2 + \gamma_2/\zeta_2 - \zeta_2) + (\zeta_2 - \gamma_2/\zeta_2 - 2)\phi_2}{(4 + 2\gamma_2/\zeta_2 - 2\zeta_2) + (2 + \zeta_2 + \gamma_2/\zeta_2)\phi_2}, \quad (23)$$

where D_1 is the diffusivity of phase 1. For 2D materials ζ_2 is given by

$$\zeta_2 = \frac{4}{\pi\phi_1\phi_2} \int_0^\infty \frac{dr_1}{r_1} \int_0^\infty \frac{dr_2}{r_2} \int_0^\pi \theta \cos(2\theta) A(r_1, r_2, \theta), \quad (24)$$

while for 3D materials,

$$\zeta_2 = \frac{9}{2\phi_1\phi_2} \int_0^\infty \frac{dr_1}{r_1} \int_0^\infty \frac{dr_2}{r_2} \int_{-1}^{+1} d(\cos\theta) P_2(\cos\theta) \times A(r_1, r_2, \theta) \quad (25)$$

with

$$A(r_1, r_2, \theta) = S_3^{(2)}(r_1, r_2, \theta) - \frac{S_2^{(2)}(r_1)S_2^{(2)}(r_2)}{S_1^{(2)}}. \quad (26)$$

Here, P_2 is the Legendre function of order 2, and θ is the angle opposite the side of the triangle of length $|\mathbf{r}_1 - \mathbf{r}_2|$. The parameter γ_2 for a d -dimensional material is given by

$$\gamma_2 = \frac{A_4^{(2)}}{(d-1)\phi_1\phi_2}, \quad (27)$$

where A_4 is a four-point microstructural parameter given by Torquato [55]. Jiao and Torquato [46] used the above expressions to obtain estimates of the diffusivity of biopolymer networks. Furthermore, Torquato [56] used analogous expansion for the effective elastic moduli, describing a similar three-point parameter η_2 that uses the two- and three-point probability functions.

Thus, the three-point correlation functions of the type computed in this paper provide us with a wide variety of options to characterize the microstructure of heterogeneous materials and even obtain accurate estimates of some of their transport and other physical properties. In addition, multiple combinations of such higher-order correlation functions can be used as target functions for reconstructing models of disordered materials based on simulated annealing [17–35,40–44], which should provide more accurate models than those produced by the two-point correlation functions.

VI. SUMMARY

Accurate characterization of microstructure of heterogeneous materials is obtained if the n -point correlation functions that describe their statistical properties can be computed. While such correlations in the limits $n = 1$ and 2 can be and

have been computed efficiently, and even measured experimentally, the same is not true for $n > 2$. In many cases, such higher-order correlation functions are required in order to develop deeper understanding of materials' properties. In this paper, we described an algorithm for computing third-order correlation functions, compared its efficiency with another algorithm proposed previously by Smith and Torquato [52], and reported on the results of extensive computation of the correlation functions for several types of heterogeneous materials, and the analysis of their correlation functions. They include the probability and cluster functions S_3 and C_3 , as well as the three-point surface and surface-surface-void correlation functions F_{SSS} and F_{SSV} , which we computed for a variety of two- and three-dimensional disordered materials and media. All the lower-order correlation functions ($n \leq 2$) were also obtained as special cases for the higher-order ones. Furthermore, the three-point correlation functions were benchmarked against the analytical expressions for a special case of packings of fully penetrable spheres. Not only is the proposed algorithm efficient, it can also be further improved, particularly for the calculation of the connectivity or cluster function $C_n^{(i)}$, in which case one would have a powerful set of microstructural descriptors for analyzing various properties of disordered materials. In the case of surface correlation functions, the accuracy of the algorithm could be further improved by exploring a recently introduced idea for converting a digitized image to a scalar field for precise identification of the two-phase interface [49].

ACKNOWLEDGMENTS

Work at the USC was supported in part by the Petroleum Research Fund, administered by the American Chemical Society, which is gratefully acknowledged. We thank the anonymous referees whose constructive comments and suggestions contributed significantly to improving the manuscript.

-
- [1] S. Torquato, *Random Heterogeneous Materials* (Springer, New York, 2002).
 - [2] M. Sahimi, *Heterogeneous Materials I* (Springer, New York, 2003).
 - [3] E. J. Garboczi and D. P. Bentz, Multi-scale analytical/numerical theory of the diffusivity of concrete, *J. Adv. Cement-Based Mater.* **8**, 77 (1998).
 - [4] D. A. Coker, S. Torquato, and J. H. Dunsmuir, Morphological and physical properties of Fontainebleau sandstone from tomographic analysis, *J. Geophys. Res.* **101**, 17497 (1996).
 - [5] M. Sahimi, *Flow and Transport in Porous Media and Fractured Rock*, 2nd ed. (Wiley-VCH, Weinheim, 2011).
 - [6] H. Feng, X. Lu, W. Wang, N. Kang, and J. W. Mays, Block copolymers: Synthesis, self-Assembly, and applications, *Polymers* **9**, 494 (2017).
 - [7] G. Xu, I. A. Dar, C. Tao, X. Liu, C. X. Deng, and X. Wang, Photoacoustic spectrum analysis for microstructure characterization in biological tissue: A feasibility study, *Appl. Phys. Lett.* **101**, 221102 (2012).
 - [8] B. Elyassi, M. Sahimi, and T. T. Tsotsis, A novel sacrificial interlayer-based method for the preparation of silicon carbide membranes, *J. Membr. Sci.* **316**, 73 (2008).
 - [9] S. Naserifar, L. Liu, W. A. Goddard, T. T. Tsotsis, and M. Sahimi, Toward a process-based molecular model of SiC membranes. 1. Development of a reactive force field, *J. Phys. Chem. C* **117**, 3308 (2013).
 - [10] S. Naserifar, W. A. Goddard, L. Liu, T. T. Tsotsis, and M. Sahimi, Toward a process-based molecular model of SiC membranes. 2. Reactive dynamics simulation of the pyrolysis of polymer precursor to form amorphous SiC, *J. Phys. Chem. C* **117**, 3320 (2013).
 - [11] M. Sahimi, *Heterogeneous Materials II* (Springer, New York, 2003).
 - [12] S. Torquato, Optimal design of heterogeneous materials, *Annu. Rev. Mater. Res.* **40**, 101 (2010).
 - [13] Y. Liu, M. S. Greene, W. Chen, D. A. Dikin, and W. K. Liu, Computational microstructure characterization and reconstruction for stochastic multiscale material design, *Comput. Aided Des.* **45**, 65 (2013).
 - [14] S. Schlüter and H.-J. Vogel, On the reconstruction of structural and functional properties in random heterogeneous media, *Adv. Water Resour.* **34**, 314 (2011).
 - [15] X. Liu and V. Shapiro, Random heterogeneous materials via texture synthesis, *Comput. Mater. Sci.* **99**, 177 (2015).

- [16] Y. Jiao, F. H. Stillinger, and S. Torquato, Modeling heterogeneous materials via two-point correlation functions. II. Algorithmic details and applications, *Phys. Rev. E* **77**, 031135 (2008).
- [17] Y. Jiao, F. H. Stillinger, and S. Torquato, A superior descriptor of random textures and its predictive capacity, *Proc. Natl. Acad. Sci. USA* **106**, 17634 (2009).
- [18] P. M. Adler, C. G. Jacquin, and J. A. Quiblier, Flow in simulated porous media, *Int. J. Multiphase Flow* **16**, 691 (1990).
- [19] P. Spanne, J.-F. Thovert, C. J. Jacquin, W. B. Lindquist, K. W. Jones, and P. M. Adler, Synchrotron Computed Microtomography of Porous Media: Topology and Transports, *Phys. Rev. Lett.* **73**, 2001 (1994).
- [20] D. Coehlo, J.-F. Thovert, and P. M. Adler, Geometrical and transport properties of random packings of spheres and aspherical particles, *Phys. Rev. E* **55**, 1959 (1997).
- [21] A. P. Roberts, Statistical reconstruction of three-dimensional porous media from two-dimensional images, *Phys. Rev. E* **56**, 3203 (1997).
- [22] C. L. Y. Yeong and S. Torquato, Reconstructing random media, *Phys. Rev. E* **57**, 495 (1998).
- [23] C. L. Y. Yeong and S. Torquato, Reconstructing random media. II. Three-dimensional media from two-dimensional cuts, *Phys. Rev. E* **58**, 224 (1998).
- [24] P. Levitz, Off-lattice reconstruction of porous media: Critical evaluation, geometrical confinement and molecular transport, *Adv. Colloid Interface Sci.* **77**, 71 (1998).
- [25] P.-E. Øren, S. Bakke, and O. J. Arntzen, Extending predictive capabilities to network models, *SPE J.* **3**, 324 (1998).
- [26] B. Biswal and R. Hilfer, Microstructure analysis of reconstructed porous media, *Phys. A (Amsterdam)* **266**, 307 (1999).
- [27] B. Biswal, C. Manwart, R. Hilfer, S. Bakke, and P.-E. Øren, Quantitative analysis of experimental and synthetic microstructures for sedimentary rock, *Phys. A (Amsterdam)* **273**, 452 (1999).
- [28] M. A. Ioannidis and I. Chatzis, On the geometry and topology of 3D stochastic porous media, *J. Colloid Interface Sci.* **229**, 323 (2000).
- [29] S. Bekri, K. Xu, F. Yousefian, P. M. Adler, J.-F. Thovert, J. Muller, K. Iden, A. Psyllos, A. K. Stubos, and M. A. Ioannidis, Pore geometry and transport properties in North Sea chalk, *J. Pet. Sci. Eng.* **25**, 107 (2000).
- [30] M. E. Kainourgiakis, T. A. Steriotis, E. S. Kikkinides, G. Romanos, and A. K. Stubos, Adsorption and diffusion in nanoporous materials from stochastic and process-based reconstruction techniques, *Colloids Surf. A* **206**, 321 (2002).
- [31] P.-E. Øren and S. Bakke, Reconstruction of Berea sandstone and pore-scale modeling of wettability effects, *J. Pet. Sci. Eng.* **39**, 177 (2003).
- [32] H. Hamzhepour and M. Sahimi, Development of optimal models of porous media by combining static and dynamic data: The porosity distribution, *Phys. Rev. E* **74**, 026308 (2006).
- [33] H. Hamzhepour, M. R. Rasaei, and M. Sahimi, Development of optimal models of porous media by combining static and dynamic data: The permeability and porosity distributions, *Phys. Rev. E* **75**, 056311 (2007).
- [34] B. Biswal, P.-E. Øren, R. J. Held, S. Bakke, and R. Hilfer, Stochastic multiscale model for carbonate rocks, *Phys. Rev. E* **75**, 061303 (2007).
- [35] C. E. Zachary and S. Torquato, Improved reconstructions of random media using dilation and erosion processes, *Phys. Rev. E* **84**, 056102 (2011).
- [36] P. Tahmasebi and M. Sahimi, Reconstruction of three-dimensional porous media using a single thin section, *Phys. Rev. E* **85**, 066709 (2012).
- [37] P. Tahmasebi and M. Sahimi, Cross-Correlation Function for Accurate Reconstruction of Heterogeneous Media, *Phys. Rev. Lett.* **110**, 078002 (2013).
- [38] P. Tahmasebi and M. Sahimi, Enhancing multiple-point geostatistical modeling. I: Graph theory and pattern adjustment, *Water Resour. Res.* **52**, 2074 (2016).
- [39] P. Tahmasebi and M. Sahimi, Enhancing multiple-point geostatistical modeling. II: Iterative simulation and multiple distance functions, *Water Resour. Res.* **52**, 2099 (2016).
- [40] Y. Jiao, E. Padilla, and N. Chawla, Modeling and Predicting Microstructure Evolution in Lead/Tin Alloy via Correlation Functions and Stochastic Material Reconstruction, *Acta Mater.* **61**, 3370 (2013).
- [41] S. Chen, H. Li, and Y. Jiao, Dynamic reconstruction of heterogeneous materials and microstructure evolution, *Phys. Rev. E* **92**, 023301 (2015).
- [42] Y. Jiao and N. Chawla, Modeling and characterizing anisotropic inclusion orientation in heterogeneous materials via directional cluster function and stochastic reconstruction, *J. Appl. Phys.* **115**, 093511 (2014).
- [43] S. Chen, A. Kirubanandham, N. Chawla, and Y. Jiao, Stochastic multi-scale reconstruction of 3D microstructure consisting of polycrystalline grains and second-phase particles from 2D micrographs, *Metall. Mater. Trans. A* **47**, 1440 (2016).
- [44] H. Li, C. S. Kaira, J. Mertens, N. Chawla, and Y. Jiao, Accurate stochastic reconstruction of heterogeneous microstructures by limited X-ray tomographic projections, *J. Microsc.* **264**, 339 (2016).
- [45] P. Tahmasebi, M. Sahimi, and J. E. Andrade, Image-based modeling of granular porous media, *Geophys. Res. Lett.* **44**, 4738 (2017).
- [46] Y. Jiao and S. Torquato, Quantitative characterization of the microstructure and transport properties of biopolymer networks, *Phys. Biol.* **9**, 036009 (2012).
- [47] B. Lu and S. Torquato, n -point probability functions for a lattice model of heterogeneous media, *Phys. Rev. B* **42**, 4453 (1990).
- [48] M. Baniassadi, M. Safdari, H. Garmestani, S. Ahzi, P. H. Geubelle, and Y. Remond, An optimum approximation of n -point correlation functions of random heterogeneous material systems, *J. Chem. Phys.* **140**, 074905 (2014).
- [49] Z. Ma and S. Torquato, Precise algorithms to compute surface correlation functions of two-phase heterogeneous media and their applications, *Phys. Rev. E* **98**, 013307 (2018).
- [50] P. Smith and S. Torquato, Computer simulation results for the two-point probability function of composite media, *J. Comput. Phys.* **76**, 176 (1988).
- [51] J. H. Conway and D. A. Smith, *On Quaternions and Octonions* (Taylor & Francis, London, 2003).
- [52] E. G. Hemingway and O. M. O'Reilly, Perspectives on Euler angle singularities, gimbal lock, and the orthogonality of applied forces and applied moments, *Multibody Syst. Dyn.* **44**, 31 (2018).

- [53] E. M. Sevick, P. A. Monson, and J. M. Ottino, Monte Carlo calculations of cluster statistics in continuum models of composite morphology, *J. Chem. Phys.* **88**, 1198 (1988).
- [54] S. Torquato and G. Stell, Microstructure of two-phase random media. III. The n-point matrix probability functions for full penetrable spheres, *J. Chem. Phys.* **79**, 1505 (1983).
- [55] S. Torquato, Effective electrical conductivity of two-phase disordered composite media, *J. Appl. Phys.* **58**, 3790 (1985).
- [56] S. Torquato, Exact Expression for the Effective Elastic Tensor of Disordered Composites, *Phys. Rev. Lett.* **79**, 681 (1997).